galaxies

MDPI

Article

The Density and Ionization Profiles of Optically Dark and High-Redshift GRBs Probed by X-ray Absorption

Eka Puspita Arumaningtyas [1,*], Hasan Al Rasyid [2], Maria Giovanna Dainotti [3,4,5] and Daisuke Yonetoku [1]

[1] Faculty of Mathematics and Physics, Kanazawa University, Kakumamachi, Kanazawa 920-1192, Ishikawa, Japan; yonetoku@astro.s.kanazawa-u.ac.jp
[2] Faculty of Engineering, Nurul Jadid University, Paiton, Probolinggo 67291, Indonesia
[3] Division of Science, National Astronomical Observatory of Japan, Osawa, Mitaka 181-8588, Tokyo, Japan; maria.dainotti@nao.ac.jp
[4] Department of Astronomical Science, The Graduate University for Advanced Studies (SOKENDAI), Osawa, Mitaka 181-8588, Tokyo, Japan
[5] Space Science Institute, Walnut Street, Boulder, CO 80301, USA
* Correspondence: ep.arumaningtyas@gmail.com; Tel.: +81-070-4429-4316

Abstract: The X-ray column density ($N_{\rm HX}$) of gamma-ray bursts (GRBs) can probe the local environment of their progenitors over a wide redshift range. Previous work has suggested an increasing trend as a function of redshift. The relevance of this current analysis relies on investigating the selection bias method, such as the effect of the X-ray spectrum in high-redshift GRBs, which complicates the measurement of small $N_{\rm HX}$; this has yet to be fully evaluated or discussed elsewhere. In this work, we evaluated these effects through simulations to define appropriate observational limits in the $N_{\rm HX}$ versus redshift plane. We then applied a one-sided nonparametric method developed by Efron and Petrosian. Within the framework of this method, we investigated the redshift dependence of $N_{\rm HX}$ and the local distribution function. Our results show that the evolution of $N_{\rm HX}$ with redshift firmly exists with a significance of more than four sigma and follows a power law of $(1+z)^{1.39(+0.22,-0.27)}$. Based on these analyses and previous studies, the GRB progenitor mass varies but is more massive in the high-redshift environment and has a higher gas column density. This suggests that part of the luminosity evolution of GRBs, which has been widely reported, may be due to the evolution of the progenitor's mass. Using the same method, we demonstrate that optically dark GRBs show a consistent evolution: $(1+z)^{1.15(+0.67,-0.83)}$. By applying the Kolmogorov–Smirnov (KS) test, it is shown that optically dark GRBs have statistically identical flux and photon index distributions compared to normal GRBs, but the $N_{\rm HX}$ is systematically larger. This result suggests that the darkness of some GRB populations is not due to an intrinsic mechanism, but rather because a higher density surrounds them.

Keywords: absorption material; intergalactic medium; gamma ray burst; Lyman-alpha; early universe

Citation: Arumaningtyas, E.P.; Al Rasyid, H.; Dainotti, M.G.; Yonetoku, D. The Density and Ionization Profiles of Optically Dark and High-Redshift GRBs Probed by X-ray Absorption. *Galaxies* **2024**, *12*, 51. https://doi.org/10.3390/galaxies12050051

Academic Editor: Phil Edwards

Received: 26 July 2024
Revised: 23 August 2024
Accepted: 26 August 2024
Published: 28 August 2024

1. Introduction

The measurement of the column density is crucial for identifying the extragalactic absorption material that accompanies the host galaxy and the local site of the GRB. The extragalactic absorption provides information about the local environment of the source and the properties of the host. In addition, it is important to note that recent work by Dainotti et al. [1,2] has drawn attention to the importance of the relationship between the neutral hydrogen column density and the redshift. Their studies emphasize that column density is the most important predictor of both X-ray and optical data, highlighting its central role in understanding the properties and behavior of various astrophysical phenomena.

The Lyman-alpha absorption lines (Ly-α) in the UV region are a powerful tool for measuring the hydrogen column density, usually expressed as $N_{\rm HI}$, in the afterglow of gamma ray bursts (GRBs). GRBs typically occur in host galaxies with high $N_{\rm HI}$, known

as damped Ly-α absorbers (DLAs), with $\log N_{\rm HI} > 20.3$ cm^{-2} [3]. This is consistent with the massive stellar progenitors of GRBs, which are known to typically be located within or near gas-rich star-forming regions such as dense molecular clouds [3,4].

In the X-ray band, we measure the column density based on the extinction observed in the low-energy spectrum. This phenomenon is primarily caused by the photoelectric effect in the medium along the line of sight. In general, we convert the total column density to an equivalent hydrogen column density ($N_{\rm HX}$) using the metallicity parameter. This indicates the total contribution of the different elements to the absorption process.

Previous research has postulated that the increase in $N_{\rm HX}$ is closely related to the redshift [5,6]. The observed increase in the $N_{\rm HX}$ trend with increasing redshift has been attributed to a distortion of dust extinction by optically dark GRBs [7]. It is noteworthy that this group of GRBs exhibits a significant proportion (20–30%) of the afterglow in the near-infrared (NIR) range [8,9].

To classify a GRB as optically dark, two classification methods have generally been used: the Jakobsson method [10] and the van der Horst method [11]. Jakobsson et al. [10] developed the classification method by comparing X-ray to optical flux ($\beta_{\rm OX}$) for all known GRBs. Using a sample of 52 GRBs, they identified five dark outbursts as outliers with $\beta_{\rm OX} < 0.5$. This threshold serves as a criterion for classifying an outburst as dark using the Jakobsson method. The van der Horst method uses X-ray flux and spectral information from Swift and classifies a GRB as dark if its $\beta_{\rm OX}$ is shallower than $\beta_{\rm X} - 0.5$.

Based on the spectral index in the afterglow theory [12,13] and related references, we expect an energy spectrum of $\nu^{-p/2}$ for the high-energy case of slow cooling. Here, p denotes the energy index of the accelerated electron. In the case of $p = 2$, the afterglow spectrum is ν^{-1}, which leads to $\beta_{\rm OX} = 1$. Assuming that the cooling frequency is between the optical and X-ray band, the spectrum progresses from $\nu^{-(p-1)/2}$ to $\nu^{-p/2}$. Therefore, the expected spectral index is $0.5 < \beta_{\rm OX} < 1$.

Although the definitions proposed by Jakobsson et al. [10] and van der Horst et al. [11] differ, both emphasize that the optical flux is weaker than the expected value based on the extended spectral index of X-rays described in standard afterglow theory.

The darkness of certain GRB groups has primarily been explained by three hypotheses. First, an intrinsic luminosity feature of the afterglow suggests the existence of optically bright and dark subclasses [14]. Second, some GRB groups may be located at high redshifts, leading to Ly-α absorption by the intergalactic medium, which hinders their detection in the R-band at the observer frame [15,16]. Finally, the darkness of certain GRB groups can be attributed to their location behind very dense material along the line of sight to the host galaxy [14,17,18].

The possibility of an increasing trend of $N_{\rm HX}$ as a function of redshift has been discussed in several previous papers [5,6,19–22]. However, these studies used forward fitting to analyze the data distribution. In this work, we applied a flux limit to select the $N_{\rm HX}$ data and then used the Efron and Petrosian method (EP method) to determine the cosmological evolution of $N_{\rm HX}$.

In contrast to many traditional methods, which assume a certain distribution of the data, the EP method is nonparametric. This means that it makes fewer assumptions about the underlying distribution, which makes it more flexible and robust for different applications. The EP method was developed specifically for dealing with truncated data, where only a subset of the data are observable due to selection effects or other limitations [23,24]. This is common in astrophysical surveys where only the brightest or closest objects are detectable.

The EP method enables the estimation of distribution functions and the investigation of correlations in the presence of truncation. This method is often used to analyze observational datasets that are subject to truncation and censoring [25–30]. Researchers such as Yu et al. [31], Petrosian et al. [32], Pescalli et al. [33], Lloyd-Ronning et al. [34], and Dainotti et al. [1] have used the EP method to determine the luminosity function $\Psi(L_0)$ and

the cosmic GRB formation rate $\rho(z)$. These studies underline the versatility and robustness of the EP method in dealing with complex astronomical data.

We have used a method that can calculate the presence or absence of correlations (in this case, $(1+z)^k$) in a set of real data distributions without being affected by the truncation of data containing unobservable regions (truncation limit) due to the flux limit and observational bias. It is important to determine a suitable truncation line. To determine the truncation in the plane N_{HX} vs. $(1+z)$, not only the flux limit of Swift XRT must be determined, but also N_{HX}, whose accuracy is simultaneously affected by the observed flux. In this case, we evaluated the flux limit with a series of spectral simulations using the respond matrix file to generate fake data and then estimated the accuracy of the N_{HX}.

2. Data Selection and Analysis Procedure

2.1. Data Selection

In this study, we analyzed the spectral properties of GRBs from the SWIFT database. We used the 404 N_{HX} values available up to GRB 240809A, which contained redshift information. We selected the time-averaged spectra of photon-counting (PC) mode for the GRBs. It is worth noting that the influence of flares on the PC mode was found to be insignificant in most cases [35]. We obtained 239 GRBs with a 90% confidence level, which means that their N_{HX} errors were less than 90%.

Table 1 provides detailed information on our GRB data sample, with each entry accompanied by redshift, N_{HX}, and flux information. We compiled a data set of 224 GRBs that met both the N_{HX} and flux criteria, with flux brighter than $10^{-12.25}$ erg $\times$ cm^{-2}s^{-1}, as described in Section 2.2. Within this dataset, we identified 30 optically dark GRBs that met both the N_{HX} and flux limit criteria.

Table 1. GRB data.

GRB Name	Redshift	N_{HX} 10^{22} cm^{-2}	N_{HX} Error 10^{22} cm^{-2}	β_{OX}	N_{HI} 10^{22} cm^{-2}	Flux 10^{-12} erg $\times$ cm^{-2}s^{-1}	Flux Error 10^{-12} erg $\times$ cm^{-2}s^{-1}
GRB050315	1.95	0.95	0.46	0.63 [3]		9.50	0.45
GRB050401* [3,a]	2.90	1.60	1.94	0.36 [3]	3.98 [3,5]	22.60	1.96
GRB050408	1.24	1.20	0.48			3.78	0.30
GRB050416A*	0.65	0.72	0.24	0.35 [6]		1.56	0.09
GRB050505	4.27	2.20	1.34	0.53 [3]	1.26 [5]	3.04	0.12
GRB050525A	0.61	0.14	0.24	0.92 [3]		5.26	0.48
GRB050802	1.71	0.24	0.24	0.51 [3]		5.22	0.21
GRB050803*	4.30	7.70	3.00	−0.15 [3]		6.17	0.29
GRB050822	1.43	0.40	0.32			3.98	0.26
GRB050922B	4.90	7.60	3.40	0.58 [3]		67.00	3.70
GRB051006	1.06	4.20	2.60	1.30 [3]		1.02	0.13
GRB051016B	0.94	0.70	0.38	0.63 [3]		1.53	0.12
GRB051022*	0.80	5.70	1.28	−0.10 [2]		15.90	0.82
GRB051111	1.55	0.58	0.66			1.29	0.12
GRB051221A	0.55	0.18	0.18			1.70	0.13
GRB060124	2.30	0.58	0.56	0.80 [3]	0.07 [5]	8.55	0.32
GRB060202*	0.79	2.10	0.52	0.20 [3]		1.61	0.09
GRB060204B*	2.34	1.80	0.84	0.47 [3]		2.32	0.14
GRB060210*	3.91	2.40	1.22	0.37 [3]	0.35 [3,5]	11.10	0.35
GRB060218	0.03	0.44	0.12			0.93	0.05
GRB060306	1.55	4.00	1.20	0.54 [3]		1.91	0.12
GRB060502A	1.51	0.42	0.44	0.53 [6]		8.79	0.66
GRB060522	5.11	3.30	5.80	0.74 [3]	0.01 [5]	2.24	0.23
GRB060604	2.68	1.00	1.06	0.75 [3]		1.32	0.09
GRB060607A	3.08	0.55	0.80	0.53 [3]	0.10 [5]	17.90	0.76
GRB060714	2.71	0.95	1.18	0.77 [3]	0.71 [5]	8.40	0.57

Table 1. *Cont.*

GRB Name	Redshift	N_{HX} 10^{22} cm^{-2}	N_{HX} Error 10^{22} cm^{-2}	β_{OX}	N_{HI} 10^{22} cm^{-2}	Flux 10^{-12} erg × cm^{-2}s^{-1}	Flux Error 10^{-12} erg × cm^{-2}s^{-1}
GRB060719*	1.53	2.90	1.04	−0.13 [3]		2.55	0.18
GRB060729	0.54	0.07	0.04	0.80 [3]		10.70	0.25
GRB060814*	1.92	4.40	0.98	−0.06 [3]		5.14	0.22
GRB060904B	0.70	0.28	0.32			2.43	0.20
GRB060908*	1.88	0.95	0.92	0.38 [3]		8.28	0.86
GRB060912A	0.94	0.21	0.32	0.62 [3]		4.29	0.42
GRB060926	3.20	3.80	5.80		3.16 [5]	1.08	0.18
GRB061007	1.26	0.74	0.32	0.79 [3]		8.62	0.50
GRB061021	0.35	0.06	0.05	0.75 [3]		3.89	0.14
GRB061121	1.31	0.73	0.24	0.64 [3]		15.60	0.61
GRB061202	2.25	15.80	4.00			15.90	0.78
GRB061222A*	2.09	5.10	1.24	−0.19 [6]		22.50	0.85
GRB070125	1.55	0.40	0.70			2.60	0.30
GRB070129	2.34	0.69	0.84	0.62 [3]		2.75	0.17
GRB070208	1.17	0.87	0.58	0.54 [6]		1.47	0.16
GRB070306*	1.50	3.60	0.88	0.23 [3]		11.60	0.54
GRB070318	0.84	0.90	0.28	0.78 [3]		2.72	0.16
GRB070328*	2.06	2.50	0.70	0.31 [3]		8.51	0.37
GRB070419A	0.97	0.43	0.66	0.87 [6]		2.33	0.43
GRB070419B*	1.96	0.76	0.56	0.25 [3]		44.40	1.91
GRB070508* [3,a]	0.82	0.82	0.46			11.20	0.72
GRB070521*	2.09	15.00	4.20	−0.06 [3]		13.50	0.83
GRB070714B	0.92	0.40	0.38			0.92	0.08
GRB070721B	3.63	1.10	1.68	0.72 [3]	0.32 [5]	21.50	1.34
GRB070724A	0.46	0.25	0.40			0.88	0.16
GRB070810A	2.17	0.91	0.90		1.41 [5]	1.93	0.17
GRB071010A	0.98	2.00	1.78	0.89 [6]		0.82	0.13
GRB071021	2.45	2.00	1.28			1.75	0.13
GRB071025	4.80	3.80	3.00	0.50 [3]		3.74	0.21
GRB071117	1.33	1.60	0.90	0.58 [3]		1.67	0.17
GRB080205	2.72	2.30	2.60	0.79 [3]		1.34	0.13
GRB080207* [2,a]	2.09	17.10	5.00	0.30 [2]		1.97	0.15
GRB080210* [1,b]	2.64	2.10	2.00		0.79 [3,5]	0.90	0.09
GRB080319A*	2.03	1.30	1.12	0.41 [6]		5.80	0.65
GRB080319B	0.94	0.13	0.11	0.52 [6]		34.40	1.42
GRB080319C* [3,a]	1.95	0.91	0.68	0.36 [6]		86.80	5.99
GRB080325* [5,a]	1.78	1.80	1.70	0.33 [4]		1.01	0.14
GRB080411	1.03	0.58	0.14			20.80	0.59
GRB080413B	1.10	0.33	0.17			5.15	0.22
GRB080430	0.77	0.49	0.16			3.60	0.18
GRB080520	1.55	2.10	2.20			1.26	0.21
GRB080602	1.82	1.40	0.74			186.00	12.30
GRB080603A	1.69	1.00	1.00			3.26	0.38
GRB080605* [3,a]	1.64	0.68	0.74			8.07	0.63
GRB080607* [3,a]	3.04	4.00	1.50		5.01 [3,5]	7.33	0.43
GRB080707	1.23	0.41	0.60			1.27	0.14
GRB080710	0.85	0.12	0.19			2.68	0.19
GRB080721	2.60	0.83	0.62		0.20 [5]	12.90	0.47
GRB080805* [1,a,b]	1.51	1.80	1.52			2.16	0.29
GRB080905A	0.12	0.23	0.38			12.80	2.17
GRB080905B	2.37	3.40	1.42		0.00 [5]	7.80	0.48
GRB080916A	0.69	0.81	0.36			5.83	0.49
GRB080928	1.69	0.34	0.42			5.62	0.34
GRB081007	0.53	0.71	0.26			5.47	0.43
GRB081109	0.98	1.40	0.46			4.26	0.26
GRB081203A	2.10	0.85	0.60		1.00 [5]	5.60	0.35
GRB081221	2.26	6.90	1.64			6.00	0.31

Table 1. *Cont.*

GRB Name	Redshift	N_{HX} 10^{22} cm^{-2}	N_{HX} Error 10^{22} cm^{-2}	β_{OX}	N_{HI} 10^{22} cm^{-2}	Flux 10^{-12} erg × cm^{-2}s^{-1}	Flux Error 10^{-12} erg × cm^{-2}s^{-1}
GRB081222	2.77	0.51	0.62		0.06 [5]	13.00	0.59
GRB090102* [1,a]	1.55	0.75	0.42			8.33	0.47
GRB090201	2.10	10.50	2.40			5.88	0.27
GRB090313	3.38	4.40	3.00		0.20 [5]	3.67	0.35
GRB090328A	0.74	0.65	0.82			2.36	0.45
GRB090404* [2,a]	3.00	12.10	3.20	0.20 [2]		3.21	0.18
GRB090417B* [2,a]	0.34	3.30	0.64	−1.90 [2]		32.60	1.57
GRB090418A	1.61	1.50	0.56			16.20	0.90
GRB090423	8.20	9.60	15.00			3.53	0.29
GRB090424	0.54	0.60	0.18			28.50	1.58
GRB090516	4.11	2.10	1.58		0.54 [5]	2.40	0.11
GRB090530	1.27	0.39	0.34			3.54	0.28
GRB090618	0.54	0.24	0.07			24.90	0.71
GRB090709A	1.80	2.20	0.70			17.70	0.79
GRB090715B	3.00	1.30	1.22		0.45 [5]	1.76	0.12
GRB090726	2.71	1.50	1.58		0.63 [5]	0.64	0.06
GRB090809	2.74	0.96	1.24		0.50 [5]	7.75	0.52
GRB090812* [1,a]	2.45	0.98	1.14		2.00 [5]	6.54	0.59
GRB090902B	1.82	2.30	1.30			3.27	0.28
GRB090926B* [1,a]	1.24	2.30	1.28			23.60	2.34
GRB091003	0.90	0.34	0.34			2.12	0.23
GRB091018	0.97	0.25	0.16			5.51	0.27
GRB091020	1.71	0.79	0.32			5.06	0.23
GRB091024	1.09	3.20	3.60			49.10	5.28
GRB091029	2.75	0.53	0.64		0.05 [5]	5.74	0.29
GRB091109A	3.08	1.30	1.98			1.93	0.20
GRB091127	0.49	0.10	0.12			80.10	5.29
GRB091208B	1.06	1.10	0.50			7.61	0.55
GRB100424A	2.46	3.40	2.60			35.50	3.77
GRB100615A* [2,a]	1.40	17.30	4.20	−0.60 [2]		24.90	1.49
GRB100621A	0.54	2.80	0.56			17.00	0.81
GRB100728A	1.57	2.60	0.78			33.30	1.31
GRB100816A	0.80	0.24	0.32			2.17	0.23
GRB100901A	1.41	0.34	0.28			11.70	0.54
GRB100906A	1.73	0.60	0.92			3.11	0.16
GRB101219A	0.72	0.81	0.82			5.88	0.91
GRB101225A	0.85	0.13	0.11			21.80	0.69
GRB110205A	2.22	0.39	0.44		0.28 [5]	4.65	0.23
GRB110422A	1.77	1.70	0.52			23.30	1.00
GRB110503A	1.61	0.24	0.22			6.19	0.25
GRB110715A	0.82	1.50	0.84			11.60	0.59
GRB110818A	3.36	1.40	1.46		0.79 [5]	3.90	0.25
GRB111008A	4.99	2.50	2.20		2.51 [5]	8.43	0.39
GRB111117A	2.21	1.50	2.40			1.18	0.19
GRB111209A	0.68	0.22	0.10			10.40	0.44
GRB111228A	0.71	0.35	0.13			9.18	0.41
GRB111229A	1.38	0.57	0.78			5.64	0.50
GRB120118B	2.94	5.70	3.40			3.99	0.35
GRB120119A	1.73	0.98	0.92		3.98 [5]	10.30	0.71
GRB120326A	1.80	0.50	0.38			9.64	0.43
GRB120404A	2.87	0.75	1.22		0.05 [5]	7.60	0.57
GRB120711A	1.41	2.00	0.56			16.80	0.67
GRB120712A	4.17	1.50	2.40		0.01 [5]	3.59	0.25
GRB120729A	0.80	0.26	0.36			2.16	0.17
GRB120811C	2.67	1.20	1.10		0.32 [5]	7.24	0.53
GRB120815A	2.36	0.71	1.24		1.12 [5]	6.29	0.48
GRB120907A	0.97	0.16	0.22			3.57	0.23
GRB120909A	3.93	2.00	2.00		0.50 [5]	9.58	0.49

Table 1. *Cont.*

GRB Name	Redshift	N_{HX} 10^{22} cm^{-2}	N_{HX} Error 10^{22} cm^{-2}	β_{OX}	N_{HI} 10^{22} cm^{-2}	Flux 10^{-12} erg × cm^{-2}s^{-1}	Flux Error 10^{-12} erg × cm^{-2}s^{-1}
GRB121024A	2.30	1.10	1.02		0.71 [5]	6.42	0.46
GRB121027A	1.77	2.00	0.62		6.31 [5]	11.20	0.61
GRB121209A	2.10	12.10	3.40			4.34	0.26
GRB121211A	1.02	0.78	0.32			3.11	0.21
GRB130420A	1.30	0.40	0.26			5.22	0.31
GRB130427A	0.34	0.11	0.08	0.95		79.30	4.02
GRB130505A	2.27	0.75	0.42		0.04 [5]	56.60	2.03
GRB130511A	1.30	0.75	0.58			1.80	0.19
GRB130603B	0.36	0.44	0.18			3.94	0.30
GRB130702A	0.14	0.05	0.08			11.40	0.88
GRB130907A	1.24	1.10	0.20			53.20	1.58
GRB130925A	0.35	3.10	0.58			75.30	3.64
GRB131004A	0.72	0.66	0.54			4.71	0.50
GRB131030A	1.29	0.42	0.32			10.30	0.64
GRB131103A	0.60	1.40	0.54			5.76	0.45
GRB131105A	1.69	2.00	0.88			3.92	0.27
GRB131108A	2.40	0.96	1.40		0.09 [5]	1.10	0.12
GRB131231A	0.64	0.28	0.22			17.70	1.66
GRB140206A	2.73	1.80	0.76		0.32 [5]	21.70	0.79
GRB140213A	1.21	0.14	0.24			13.20	0.52
GRB140301A	1.42	0.85	0.88			1.90	0.27
GRB140304A	5.28	4.10	4.80			25.30	1.69
GRB140419A	3.96	1.20	1.04		0.00 [5]	11.60	0.39
GRB140423A	3.26	1.10	0.92		0.03 [5]	8.49	0.43
GRB140430A	1.60	0.74	0.94		0.63 [5]	1.72	0.14
GRB140506A	0.89	0.88	0.32			13.10	0.61
GRB140508A	1.03	0.25	0.42			6.94	0.90
GRB140512A	0.72	0.28	0.13			36.00	1.21
GRB140515A	6.32	4.30	6.60		0.00 [5]	4.44	0.33
GRB140518A	4.71	2.90	3.20		0.45 [5]	6.33	0.47
GRB140629A	2.27	0.80	0.52		1.00 [5]	3.11	0.16
GRB140703A	3.14	1.00	1.60		0.79 [5]	10.70	0.62
GRB140903A	0.35	0.18	0.16			3.70	0.32
GRB140907A	1.21	0.54	0.66			2.87	0.19
GRB141109A	2.99	2.10	1.44		1.26 [5]	8.30	0.56
GRB141121A	1.47	0.42	0.42			11.50	0.83
GRB141220A	1.32	0.38	0.54			3.09	0.35
GRB150206A	2.09	1.10	0.44		0.50 [5]	11.20	0.45
GRB150314A	1.76	1.80	0.66			55.80	3.03
GRB150323A	0.59	0.56	0.38			3.37	0.38
GRB150403A	2.06	0.81	0.32		0.63 [5]	28.40	0.82
GRB150821A	0.76	2.20	0.70			8.24	0.60
GRB151021A	2.33	2.30	0.86		1.58 [5]	11.60	0.64
GRB151027A	0.81	0.43	0.13			34.90	1.32
GRB151027B	4.06	3.30	4.20		0.03 [5]	4.00	0.35
GRB151031A	1.17	1.00	0.68			1.69	0.19
GRB160131A	0.97	0.40	0.17			8.04	0.28
GRB160425A	0.56	1.00	0.34			4.27	0.29
GRB160509A	1.17	2.60	0.70			17.60	0.69
GRB160623A	0.37	2.40	0.96			39.70	2.25
GRB160804A	0.74	0.20	0.18			2.70	0.20
GRB161014A	2.82	1.80	1.68		0.25 [5]	17.10	1.17
GRB161117A	1.55	0.82	0.36			14.00	0.67
GRB161219B	0.15	0.20	0.05			38.90	1.34
GRB170113A	1.97	0.92	0.58			16.50	0.76
GRB170519A	0.82	0.37	0.17			8.11	0.44
GRB170705A	2.01	1.20	0.40			19.20	0.74
GRB180205A	1.41	0.50	0.56			8.95	0.80
GRB180325A	2.25	1.30	0.76		2.00 [5]	15.70	0.93
GRB180620B	1.12	0.50	0.26			19.50	1.16

Table 1. *Cont.*

GRB Name	Redshift	N_{HX} 10^{22} cm^{-2}	N_{HX} Error 10^{22} cm^{-2}	β_{OX}	N_{HI} 10^{22} cm^{-2}	Flux 10^{-12} erg × cm^{-2}s^{-1}	Flux Error 10^{-12} erg × cm^{-2}s^{-1}
GRB180624A	2.85	1.00	1.54		3.16 [5]	2.29	0.21
GRB180720B	0.65	0.34	0.11			207.00	7.86
GRB180728A	0.12	0.07	0.06			41.20	1.06
GRB181010A	1.39	2.30	0.64			8.17	0.42
GRB181020A	2.94	0.75	0.62		1.58 [5]	26.30	1.08
GRB190114A	3.38	1.50	2.00			6.52	0.36
GRB190114C	0.42	8.00	1.10			37.40	1.35
GRB190829A	0.08	1.40	0.19			106.00	3.50
GRB191011A	1.72	0.67	0.68			2.17	0.21
GRB201015A	0.43	0.58	1.02			1.69	0.30
GRB201020B	0.80	0.71	0.88			6.27	1.05
GRB201221A	5.70	8.30	13.20			4.68	0.49
GRB210204A	0.88	0.61	0.82			4.03	0.65
GRB210210A	0.71	0.12	0.19			14.80	1.03
GRB210321A	1.49	0.88	0.90			4.28	0.44
GRB210619B	1.94	0.70	0.52			76.30	2.69
GRB210702A	1.16	0.23	0.18			30.10	1.10
GRB211024B	1.11	0.30	0.13			103.00	3.90
GRB211207A	2.27	1.60	1.92			1.36	0.19
GRB221009A	0.15	1.40	0.76			229.00	17.90
GRB230325A	1.66	1.70	1.22			2.71	0.34
GRB231118A	0.83	0.89	0.44			45.00	4.00
GRB240419A	5.18	11.30	13.20			2.20	0.33

[1] Greiner et al. [9]; [2] Chrimes et al. [36]; [3] Fynbo et al. [37]; [4] Hashimoto et al. [38]; [5] Tanvir et al. [3]; [6] Perley et al. [17]. AuthThe [*] after GRBs name indicate optically dark GRB. AuthIndicators for Darkness Classification Method : [a]. Jakobsson [b]. van der Horst.

2.2. Analysis Procedure

Our study focuses on the X-ray absorption properties of Swift GRBs with known redshift, including the selection bias in flux-limited data. We used simulations to set lower limits on detectable N_{HX} values. We found that small N_{HX} values can only be accurately measured for bright and low-shifted afterglows. In contrast, for high-shifted GRBs, we can only accurately measure larger N_{HX} values due to the redshift effect on the X-ray photon energy, which shifts to lower energies with increasing redshift by $(1+z)^1$. Consequently, large N_{HX} values can be measured for GRBs with high redshift.

In this study, we used an absorbed power-law function to account for each power-law decay phase. The absorption was modeled with two components, namely, phabs and zphabs. The first component was fixed to the Galactic value, while the second component was fixed to the redshift of the host galaxy and the assumed solar metallicity. These modeling strategies allowed us to accurately describe the observed spectra and extract valuable information from our data.

We generated truncation lines for the N_{HX} redshift plane using the "fakeit" command in the XSPEC software, ver. 12, created by Keith Arnaud, Ben Dorman, and Craig Gordon. This software created in NASA, Greenbelt, MD, USA. The software is accessed online from https://heasarc.gsfc.nasa.gov/lheasoft/ (accessed on 25 July 2024). For the simulated spectra, we assumed a photon index of two for the afterglow spectrum and a galactic column density of 2.1×10^{21} cm^{-2}, the average value of all samples. The detection sensitivity of the SWIFT XRT telescope is 2×10^{-14} erg × cm^{-2}s^{-1} in 10^4 s [39]. To ensure that our simulations are relevant to our GRBs database, we determined the exposure time as a fixed parameter, based on the average exposure time from the GRBs database, which is 10^3 s. We then fitted the simulated spectra with the input model function and extracted the best N_{HX} value and its error.

A total of 495,000 simulations were performed by varying the redshift ($1 \leq z \leq 9$), dividing the X-ray column density into 11 levels ($10^{20} \leq N_{HX} \leq 10^{22}$). Our flux limit exceeds the sensitivity of the SWIFT instrument, which is 10^{-14} in 10^4 s [39]. However, the minimum flux in our 404 GRBs database is 10^{-13}. It is important to note that obser-

vations under the flux limits of 10^{-13} generally have lower signal-to-noise ratios, which can decrease the quality of the data. In this case, we simulated the flux into 50 levels ($10^{-13} \leq F \leq 10^{-10}$), with 100 trials for each combination. The cut-off line, shown in the left panel of Figure 1 for each redshift, was determined by selecting cases where the relative error of N_{HX} was less than 0.9. Later, we created the contour plot based on the difference between the average N_{HX} value and the value calculated for different redshift ranges. The flux limit for each N_{HX} value was determined by finding the cross-section between x (logarithmic of flux limit) and y (X-ray column density) in the region where we cannot define the contour.

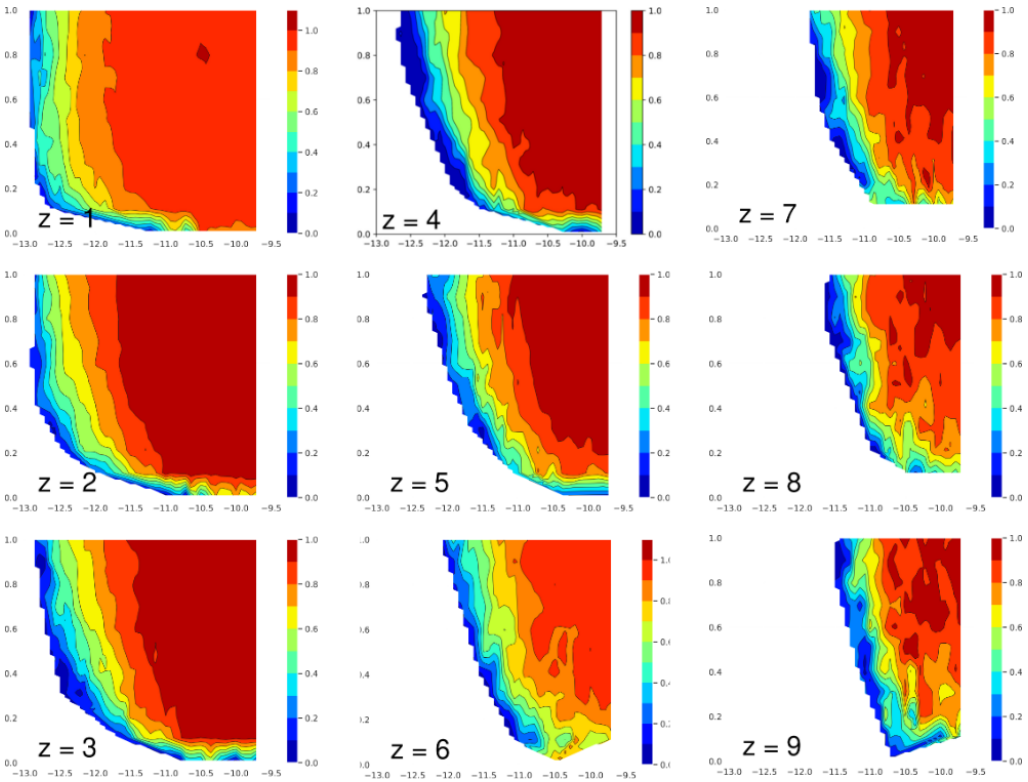

Figure 1. The contour plot of the simulated log flux (x-axis) versus N_{HX} (y-axis) for different redshift range.

We analyzed 404 GRBs from the Swift database with available redshift and absorbed flux data. We obtained 239 GRBs with a 90% confidence level. After applying the flux limit, we obtained 224 data points where both N_{HX} and flux were within the flux limit. To avoid selecting fewer absorbed GRBs and excluding the most absorbed ones, we set a high flux limit of $10^{-12.25}$ erg $\times$ cm^{-2}s^{-1}, which preserved a high percentage (89%) of the data sample.

The data samples are constrained by truncation, including the flux limit caused by detector sensitivity. We used a one-sided nonparametric method developed by Dainotti et al. [40] to estimate the redshift evolution of the X-ray column density. This method, derived from Efron and Petrosian [23,24], does not involve the correlation of the parameters. Instead, it evaluates the correlation between N_{HX} and the redshift. We used the lower bound of the flux limit for this analysis. By applying this method, we calculated the corrected distribution of N_{HX}.

We compared the cumulative density rate of the optically dark GRBs with the rest of the GRB data sample of the SWIFT XRT database. We identified the optically dark GRBs and created a reliable list by applying the flux limit criteria. We then used the Kolmogorov–Smirnov test to compare the flux, photon index, and N_{HX} distributions of the two datasets to determine whether they were from the same population.

3. Result

3.1. Evolution of the redshift of N_{HX}

We created a model of the GRB spectrum that includes the absorption of both galactic and host redshift by using the power-law absorption model (phabs) and the redshifted power-law absorption model (zphabs).

We used the "fakeit" command in XSPEC to generate simulated spectra, taking into account parameter ranges for the flux ($10^{-13} \leq F \leq 10^{-10}$ with 50 steps) and N_{HX} ($10^{20} \leq N_{HX} \leq 10^{22}$ with 11 steps). Figure 1 shows the contour plot of our simulated flux versus N_{HX} for different redshift ranges.

Figure 2 (left panel) illustrates an apparent increase of 245 N_{HX} with redshift (including the outlier). Optically dark GRBs are represented by red triangles, while others are indicated by black dots. The green crosses represent the N_{HX} that did not fullfil the flux limit requirement. To interpret the data distribution accurately, it is crucial to define a truncation line that is dependent on the flux limit.

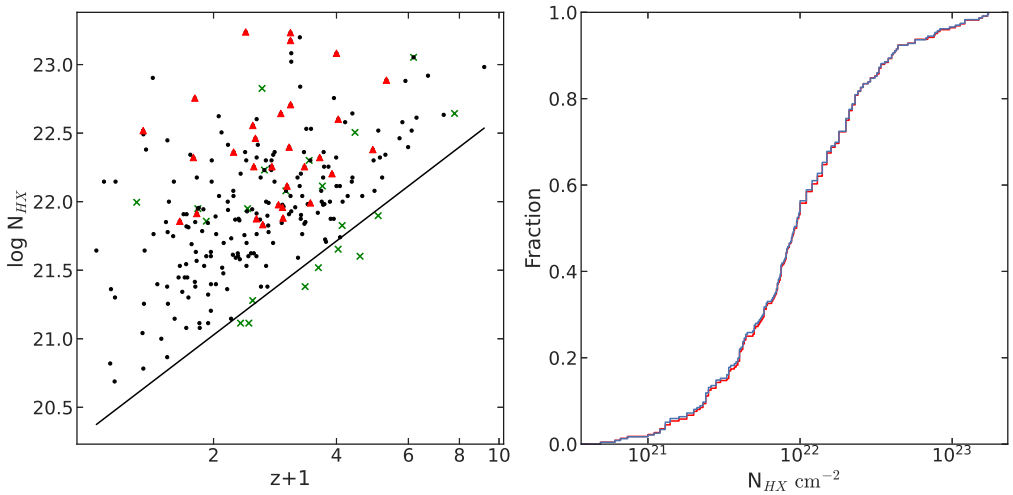

Figure 2. The left panel illustrates the correlation between N_{HX} and the redshift in our sample of 245 GRBs. Optically dark GRBs are represented by red triangles, while black dots indicate non-dark GRBs. The green crosses represent data points outside the flux limit. The solid line represents the assumed sensitivity limit for the column density given by the flux limit. The right panel shows the cumulative distribution of GRB data after the removal of certain entries (shown in blue) and the distribution of remaining entries (shown in red), resulting in a *p*-value of 0.996.

When we exclude data due to the flux limit, it is important that the remaining data distribution retains the original distribution. We created cumulative distributions for data selected with different flux limits and compared them to the original distribution. Figure 2 (right panel) shows an example of the N_{HX} distribution for a flux limit of $10^{-12.25}$, with a random probability of the KS test of 0.996.

We used a one-sided parametric approach developed by Efron and Petrosian to evaluate the evolution of X-ray column density with redshift in GRB data [23,24,40]. We have assumed that the evolution of the redshift follows a simple formula, namely, $\propto (1+z)^k$. By varying k from 0 to 2.5 with a step size of 0.1, we evaluated the randomness of the data distribution and calculated the test statistic τ. Figure 3 shows the τ values plotted against the N_{HX} evolution index k within a three-sigma error range. We identified the optimal value of k as k_0 at $\tau = 0$, which corresponds to an evolution index of $k = 1.39^{(+0.22,-0.27)}$ within a one-sigma range. Using the same method, we determined the evolution properties of optically dark GRBs and obtained an evolution index of $k = 1.15^{(+0.67,-0.83)}$ within a one-sigma range.

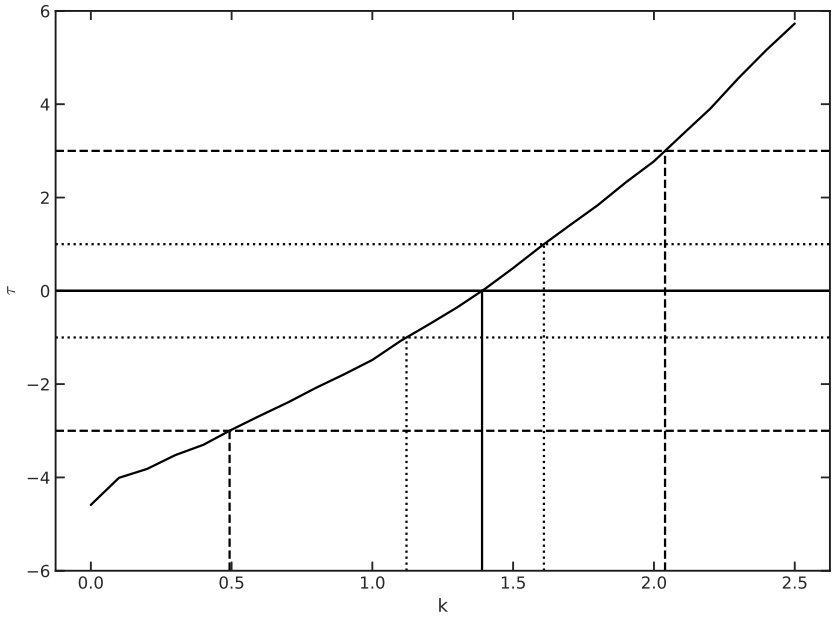

Figure 3. The test statistic τ is plotted against the evolution index k for the optimal value of 1.39. The one-sigma range is from 1.12 to 1.61, while the three-sigma range is from 0.49 to 2.04.

Figure 4a,b illustrate the distribution of the logarithm of column density ($\log(N_{\rm HX})$) at a redshift of zero $(z = 0)$ for normal GRBs and optically dark GRBs. This distribution, shown as a solid line, has been corrected for selection biases and takes into account the redshift evolution of the column density. Using the redshift evolution factor of $(1+z)^{1.39}$ derived from Figure 4a, we can extrapolate the $N_{\rm HX}$ of the normal GRBs distribution at any redshift. Using the same method, we can determine the $N_{\rm HX}$ distribution of the optically dark GRB using the redshift evolution factor of $(1+z)^{1.15}$ derived from Figure 4b.

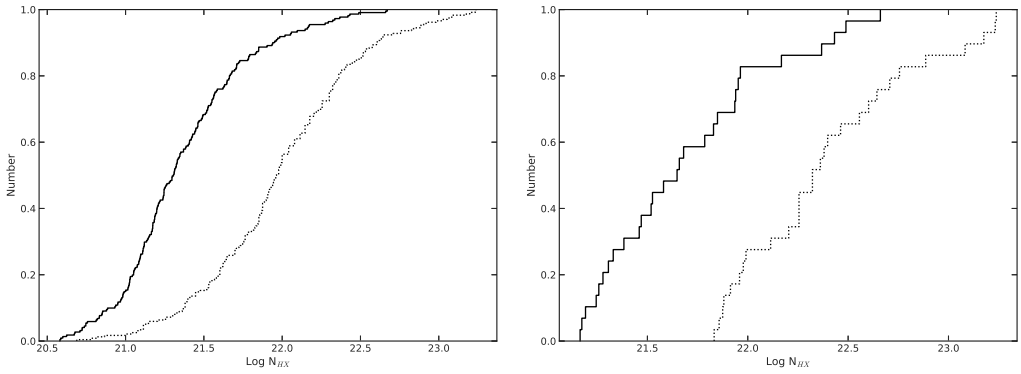

(**a**) (**b**)

Figure 4. The normalized cumulative distribution of the X-ray column density ($N_{\rm HX}$) is shown for corrected (solid lines) and uncorrected (dashed lines) GRBs for normal GRBs, shown in (**a**), and optically dark GRBs, shown in (**b**).

3.2. Properties of Optically Dark GRBs

Figure 2 (left panel) shows that optically dark GRBs tend to have higher $N_{\rm HX}$ values compared to other GRBs in the same redshift ranges. This difference is probably due to a dustier environment. The hosts of optically dark GRBs are characterized by a higher mass, a redder color, and a higher luminosity [9,36,41]. In addition, the distinct extinction of the host frame is higher, with $AV > 1 mag$ [42]. This evidence supports the conclusion that dust obscuration is the cause of the optical darkness, which in turn leads to higher $N_{\rm HX}$ values.

Figure 2 (left panel) shows that GRBs with the same high N_{HX} can be either bright or optically dark. A possible explanation for this effect is the variation in the metallicity of the absorption material, as previously studied by Chrimes et al. [36], in host galaxies with higher dust content and solar metallicity. This idea is also supported by cases such as GRB 020819 [43] and GRB 051022 [44], both of which exhibit solar metallicity and where no optical nor near-infrared afterglow was detected. The increased metallicities leading to increased mass loss could contribute to significant extinction during the lifetime of the progenitor [45]. These results suggest that metallicity may play a critical role in determining the observed properties of GRBs, particularly in X-ray absorption.

After applying a flux limit of $10^{-12.25}$ erg $\times$ cm^{-2}s^{-1} to the GRB data, the results shown in Figure 5 emphasize and complement the results shown in Figure 2 (left panel). Figure 5 represents the results of Kolmogorov–Smirnov tests conducted to compare three different properties of two groups of gamma ray bursts, optically dark GRBs and the remaining GRBs, after applying a flux limit of $10^{-12.25}$ erg $\times$ cm^{-2}s^{-1}. First, Figure 5a displays the distributions of the time-averaged flux (calculated within 12 hours of the outburst) for both groups. The KS test comparing these distributions yields a statistic of 0.12 and a p-value of 0.76. This suggests that the time-averaged flux distributions of optically dark GRBs and the remaining GRBs are not statistically different. Next, Figure 5b compares the photon indices of the two groups. The KS test results in a statistic of 0.14 and a p-value of 0.63, again indicating no statistically significant difference between the photon index distributions. Finally, Figure 5c presents the distributions of the X-ray column density (N_{HX}) for both groups. In this case, the KS test yields a statistic of 0.38 and a p-value of 0.00065. This low p-value indicates a statistically significant difference between the N_{HX} distributions of optically dark GRBs and the remaining GRBs.

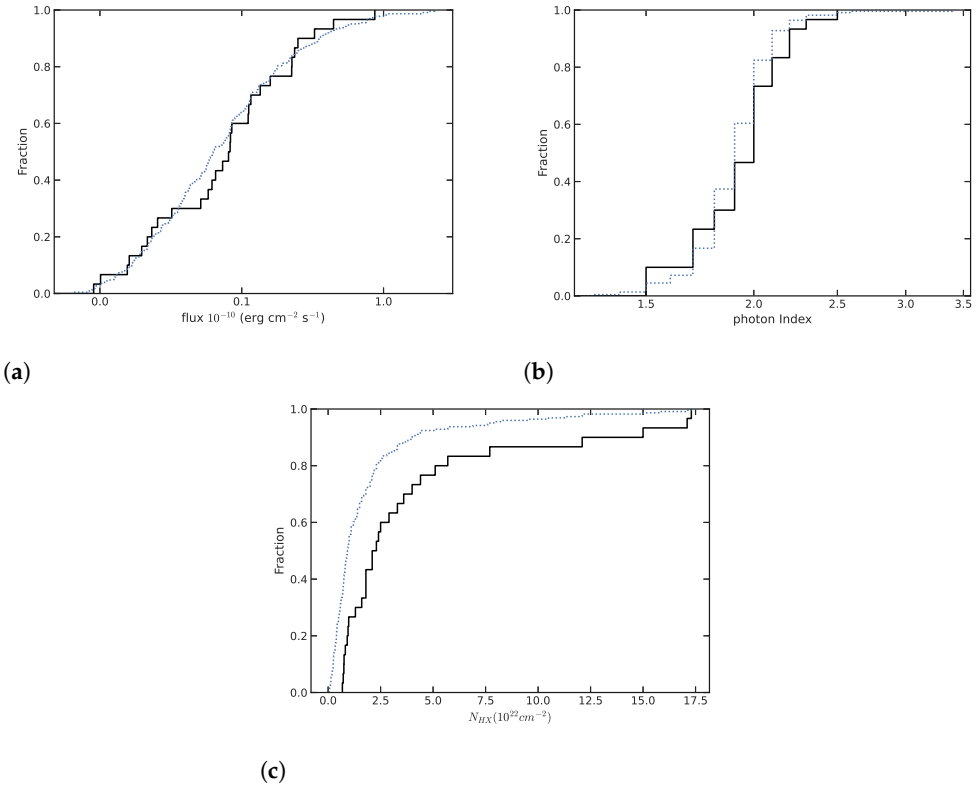

Figure 5. This figure shows the results of the Kolmogorov–Smirnov test (KS) for two groups: optically dark GRBs (black) and the remaining GRBs (blue). (**a**) shows the distribution of the time-averaged flux for the two groups, giving a KS test statistic of 0.12 and a p-value of 0.76. In (**b**), the photon index of the two groups is compared, resulting in a KS test statistic of 0.14 and a p-value of 0.63. The distribution of the X-ray column density (N_{HX}, right) with a KS test statistic of 0.38 and a p-value of 0.00065 is represented in (**c**).

3.3. The N_{HX} of GRBs with High Redshift

GRBs with a high redshift generally exhibit a faint afterglow due to their large distance. If the wavelength of the Ly-α break at $z > 5$ is more than 730 nm, observation in the optical band becomes difficult. Therefore, its afterglow is typically detected by telescopes with an aperture of more than 2 meters and a near-infrared detector. The early afterglow can only become visible when these telescopes start observing and are identified as optically dark GRBs. For example, the afterglows of the highly displaced GRB 050904 and GRB 90429B were identified in the near-infrared about 3 hours after the outburst [46].

Although the number of samples is limited, 13% of the optically dark GRBs are from high redshifts, which have a similar environment to optically dark GRBs at $z < 5$. Optically dark GRBs account for 20–30% of all events, and, of these, 13%, i.e., 2.6–3.9% of the total, could represent undetected high-redshift events.

Although optically dark and high-shift GRBs share the feature of a high N_{HX}, the origin of the absorption could be different. Due to the limited energy bandwidth of the Swift XRT (0.3–10 keV), the measurement of N_{HX} in high-redshift GRBs is a major challenge.

4. Discussion and Conclusions

The column density of the GRB population showed a wide range of characteristics. The relevance of the current analysis lies in its focus on investigating the selection bias method, particularly in examining the effects of the X-ray spectrum in high-redshift GRBs. This aspect of the analysis is crucial because it addresses the challenges associated with measuring the small values of column density in these distant and energetic events. The complexities and implications of this measurement difficulty have not yet been fully evaluated or discussed in other studies, making this analysis a novel and significant contribution to the field. It is relevant to note that the work of Dainotti et al. [1,2] recently highlighted the importance of the relation between column density and redshift, with column density as the most important predictor for both the X-rays and optical data. Moreover, in contrast to many other forward-fitting methods used to solve this problem, we used the Efron–Petrosian method, which allows a nonparametric determination of these quantities. In this work we have obtained a precise description of the distribution of these properties—in particular, their cosmological evolution. Our results confirm the evolution of N_{HX} with the redshift as $(1+z)^{1.39}$. Using the same method, we obtained a similar trend for optically dark GRBs as $(1+z)^{1.15}$. Indeed, the fact that we find similar results to previous studies is not trivial since the relationship between N_{HX} and the redshift could have been the result of selection biases rather than intrinsic physics.

Our results on the evolution of N_{HX} indicate that we might observe either metal content ejected by the progenitor star or a gas component largely unaffected by cosmic metallicity evolution. Higher metallicity generally means a greater abundance of heavy elements in the surrounding medium. Heavier elements are known to absorb X-rays more efficiently than lighter elements. These results suggest that metallicity may play a critical role in determining the observed properties of GRBs, particularly in X-ray absorption.

In environments with higher metallicity, star clusters experience greater mass loss compared to those in lower-metallicity environments [45]. This is because heavier elements in stellar atmospheres enhance the efficiency of line-driven winds, leading to more substantial mass loss over time. This process can contribute to significant extinction in the surrounding medium during the progenitor's lifetime, as the expelled material enriches the interstellar medium with heavy elements and increases the overall density of the surrounding gas and dust. The increased extinction due to higher metallicity-driven mass loss can influence the observed properties of the X-ray and optical GRB emission.

However, to use metallicity as an explanation for the evolution of N_{HX}, it is important also to consider the evolution of metallicity itself. For example, host GRBs at redshift $z < 0.4$ show a subsolar metallicity cut-off, approximately $0.4(Z\odot)$ [47]. Evidence suggests that GRBs at high redshift preferentially occur in low-metallicity systems, with no clear indication of an increased metallicity with redshift [48,49]. By utilizing a lower metallicity

of 0.07 ± 0.05 $Z/Z\odot$, the calculated X-ray column density is reduced by 0.7–0.9% [6]. It appears that the evolution of N_{HX} is not associated with the metals present in the general interstellar medium of the host galaxy. The variation in metallicity may help explain why GRBs with the same high N_{HX} can appear either bright or optically dark, as demonstrated in Figure 2 (left panel).

In galaxies with intense star formation, high X-ray column densities are often attributed to the dense interstellar medium and the substantial amounts of dust and gas produced by stellar processes. For GRB hosts, a high star formation rate (SFR) may suggest a young, actively forming galaxy with significant dust and gas content. Additionally, high SFRs can be associated with active galactic nuclei (AGNs) or starburst activity, where intense processes may lead to the ejection of gas and dust into the surrounding medium. This interaction can result in higher N_{HX} values, as the burst's X-ray emission interacts with the dense material in the host galaxy. Previous studies have indicated that GRBs exhibit an unusually high formation rate at low redshifts, exceeding the corresponding SFR by more than an order of magnitude [1,50]. However, evidence between redshifts 1 and 3 aligns with an almost constant SFR, with a noticeable decline beyond this range [32,51]. Evidence indicates that those at ($z > 4$) are less dusty than those at lower redshift, with an extinction value of $A_v < 0.5$ mag [52]. Therefore, the evolution in N_{HX} cannot be explained by the increasing dust content at higher redshift. The cosmological evolution of N_{HX} can be attributed to the accumulation of ionized and highly diffused intergalactic medium (IGM) [5]. This intriguing phenomenon needs further investigation. Despite this, the scatter displayed by N_{HX} poses a considerable challenge to a straightforward interpretation within the confines of the IGM model. This complexity suggests that, while the IGM may contribute to the overall trend, additional factors and mechanisms may play a role in shaping the observed scatter of N_{HX}, for example, the local interstellar medium (ISM) of the host galaxy. Results from our simulation suggested that 13% of GRBs remain in high-density (10^4 cm^{-3}) low-temperature star-forming regions, whereas 87% of GRBs occur in low-density ($\sim$ 10–2.5 cm^{-3}) high-temperature regions heated by supernovae [53]. A high percentage of the GRBs remain in a low-density environment, contrasting with the high N_{HX} and the evolution with redshift. This contradiction can be explained by certain different models of dust and star distribution in a very clumpy ISM [54].

The stellar initial mass function (IMF) at high redshifts is a crucial but not yet fully understood aspect of early cosmic events. If LGRBs originate from massive stars, evidence suggests that the IMF in the early universe may have been skewed towards larger stellar masses. Some evidence indicates that the early universe likely favored the formation of more massive stars than we observe today [55,56]. Population III stars with masses ranging from as low as a few to several tens of $M\odot$ [57] to more than a hundred $M\odot$ [58] are considered viable progenitors for long-duration GRBs at high redshift [59]. Simulation results have found that the expected fraction of Pop III GRBs is $\sim$ 10% of the full GRB population at $z > 6$ and becomes as high as 40% at $z > 10$ [60].

GRBs are detectable at very high redshifts, potentially beyond $z \approx 10$ [61], and especially now with the new observations of high-z galaxies observed at $z = 14$, which can host population III stars. Their observed properties can provide direct information about the universe's conditions during the epoch of reionization (EoR), which occurred roughly between $z \approx 6z$ and $z \approx 10z$. Only if the average escape fraction is sufficiently high, i.e., $fesc$ at least 0.1–0.2 [62], it is probable that this phase change was primarily caused by EUV starlight.

Following Chen et al. [63], the average escape fraction is inversely proportional to the column density. The total escape fraction inferred from the GRB column density is one magnitude lower than the expected value [3]. There is evidence from simulations that GRBs with the same massive progenitor can remain in the star-forming region. Simultaneously, another population may likely migrate to a less dense environment [53]. This could occur due to significant relative motions between stars and their birth clouds. Numerical models suggest that a relative motion of 10 kms^{-1} between a star and its birth cloud could result

in a displacement of 100 pc over a lifetime of 10 Myr. Runaway OB stars typically exhibit velocities relative to their birth clouds of around 20 kms^{-1} [64]. Consequently, runaway OB stars have played a significant role in displacing GRBs from their birth clouds. The presence of GRBs in hot, low-density environments is also influenced by supernova heating from earlier supernovae within the birth clouds. These two effects contribute almost equally to placing most GRBs in low-density, high-temperature regions [53]. Le Floc'h et al. [65] demonstrate that GRB 980425, which occurred in a nearby ($z = 0.0085$) SBc-type dwarf galaxy, appears to be displaced by 0.9 kpc from the nearest HII region. The evolution of N_{HX} suggests that there is a population of GRBs with low column density (less than log 19) that have been missed in detections.

The implication of undetected optically dark GRBs can lead to a misinterpretation of the GRB's host galaxies metallicity. The metallicity distribution derived from analyzing optical afterglow spectroscopy might not fully represent the true distribution of metallicities found in the entire universe. This potential discrepancy arises because the method relies heavily on the observations of optical afterglows. However, there may be a bias in this observational approach: it tends to favor detecting afterglows from sources that exhibit lower metallicities, while bursts associated with higher metallicities might be less visible or even undetectable in optical wavelengths. This situation can occur because some bursts, particularly those with higher metallicity, might be optically dark GRBs. Consequently, the observed distribution of metallicities based on these optical afterglows could underrepresent the actual range of metallicities present, especially if many high-metallicity bursts are not identified or are missed altogether. This limitation underscores the need for complementary observational strategies or technologies to capture a more accurate and comprehensive picture of the underlying metallicity distribution in the universe. THESEUS will identify more than 20 events at $z > 6$ in 3.5 years of nominal operation, thus providing a much larger sample of high-redshift GRBs than achieved so far [66]. High-z Gundam mission might be comparable to THESEUS (5 event per year) [67]. SVOM is already operational, equipped with the 4–150 keV wide-field trigger camera and has sensitivity to a wide variety of GRBs, including those at high redshifts. It is expected to detect around 80–100 GRBs per year [68].

In summary, we used simulations to establish observational flux limits and applied a one-sided nonparametric method by Efron and Petrosian to understand the correlation between the N_{HX} and redshift. We found a significant evolution of N_{HX} with redshift, following a power law of $(1+z)^{1.39(+0.22,-0.27)}$. For optically dark GRBs, a similar evolution of $(1+z)^{1.15^{(}+0.67,-0.83)}$ was obtained. A Kolmogorov–Smirnov test showed that optically dark GRBs have similar flux and photon index distributions as normal GRBs, but a larger N_{HX}, indicating that their darkness results from a higher surrounding density rather than an intrinsic mechanism. The evolution of N_{HX} suggests that GRB progenitors are more massive and have higher gas column densities at higher redshifts, potentially contributing to GRB luminosity evolution.

Author Contributions: Eka Puspita Arumaningtyas as E.P.A., Hasan Al Rasyid as H.A.R., Maria Giovanna Dainotti as M.G.D. and Daisuke Yonetoku as D.Y. E.P.A. and D.Y.: conceptualization; E.P.A., M.G.D. and D.Y.: methodology; M.G.D. and D.Y.: validation; E.P.A., M.G.D. and D.Y.: formal analysis; E.P.A. and H.A.R.: data curation; E.P.A.: writing—original draft preparation; E.P.A., H.A.R., M.G.D. and D.Y.: writing—review and editing; E.P.A. and H.A.R.: software implementation and visualization; M.G.D. and D.Y.: supervision; D.Y.: funding acquisition. All authors have read and agreed to the published version of the manuscript.

Funding: This research was supported by Project for Remarkable Ph.D. Students in Next Generation of Kanazawa University, JSPS KAKENHI Grant Numbers 23H04898 (DY), 21H01090 (DY), 20K20525 (DY), and Sakigake project 2022 of Kanazawa University.

Data Availability Statement: We analyzed the spectral properties of GRBs from the SWIFT-XRT GRB Catalogue (https://www.swift.ac.uk/xrt_live_cat/ (accessed on 16 August 2024.)).

Conflicts of Interest: The authors declare no conflicts of interest. The funders had no role in the design of the study; in the collection, analyses, or interpretation of data; in the writing of the manuscript; or in the decision to publish the results.

References

1. Dainotti, M.G.; Narendra, A.; Pollo, A.; Petrosian, V.; Bogdan, M.; Iwasaki, K.; Prochaska, J.X.; Rinaldi, E.; Zhou, D. Gamma-Ray Bursts as Distance Indicators by a Statistical Learning Approach. *Astrophys. J. Lett.* **2024**, *967*, L30. [CrossRef]
2. Dainotti, M.G.; Taira, E.; Wang, E.; Lehman, E.; Narendra, A.; Pollo, A.; Madejski, G.M.; Petrosian, V.; Bogdan, M.; Dey, A.; et al. Inferring the Redshift of More Than 150 GRBs with a Machine-learning Ensemble Model. *Astrophys. J. Suppl. Ser.* **2024**, *271*, 22. [CrossRef]
3. Tanvir, N.R.; Fynbo, J.P.U.; de Ugarte Postigo, A.; Japelj, J.; Wiersema, K.; Malesani, D.; Perley, D.A.; Levan, A.J.; Selsing, J.; Cenko, S.B.; et al. The Fraction of Ionizing Radiation from Massive Stars That Escapes to the Intergalactic Medium. *Mon. Not. R. Astron. Soc.* **2019**, *483*, 5380–5408. [CrossRef]
4. Jakobsson, P.; Fynbo, J.P.U.; Ledoux, C.; Vreeswijk, P.; Kann, D.A.; Hjorth, J.; Priddey, R.S.; Tanvir, N.R.; Reichart, D.; Gorosabel, J.; et al. H I Column Densities of $z > 2$ *Swift* Gamma-Ray Bursts. *Astron. Astrophys.* **2006**, *460*, L13–L17. [CrossRef]
5. Rahin, R.; Behar, E. Cosmological Evolution of the Absorption of ϒ-ray Burst X-Ray Afterglows. *Astrophys. J.* **2019**, *885*, 47. [CrossRef]
6. Dalton, T.; Morris, S.L. Using Realistic Host Galaxy Metallicities to Improve the GRB X-ray Equivalent Total Hydrogen Column Density and Constrain the Intergalactic Medium Density. *Mon. Not. R. Astron. Soc.* **2020**, *495*, 2342–2353. [CrossRef]
7. Watson, D.; Jakobsson, P. Dust extinction Bias in the Column Density Distribution of Gamma-ray Bursts: High Column Density, Low-Redshift Grbs Are More Heavily Obscured. *Astrophys. J.* **2012**, *754*, 89. [CrossRef]
8. Fynbo, J.U.; Gorosabel, J.; Dall, T.H.; Hjorth, J.; Pedersen, H.; Andersen, M.I.; Møller, P.; Holland, S.; Smail, I.; Kobayashi, N.; et al. The Optical Afterglow and Host Galaxy of GRB 000926. *Astron. Astrophys.* **2001**, *373*, 796–804. [CrossRef]
9. Greiner, J.; Krühler, T.; Klose, S.; Afonso, P.; Clemens, C.; Filgas, R.; Hartmann, D.H.; Yoldaş, A.K.; Nardini, M.; Estay, F.O.; et al. The Nature of "Dark" Gamma-Ray Bursts. *Astron. Astrophys.* **2011**, *526*, A30. [CrossRef]
10. Jakobsson, P.; Hjorth, J.; Fynbo, J.P.U.; Watson, D.; Pedersen, K.; Björnsson, G.; Gorosabel, J. Swift Identification of Dark Gamma-Ray Bursts. *Astrophys. J.* **2004**, *617*, L21–L24. [CrossRef]
11. van der Horst, A.J.; Kouveliotou, C.; Gehrels, N.; Rol, E.; Wijers, R.A.M.J.; Cannizzo, J.K.; Racusin, J.; Burrows, D.N. OPTICAL CLASSIFICATION OF GAMMA-RAY BURSTS IN THE *SWIFT* ERA. *Astrophys. J.* **2009**, *699*, 1087–1091. [CrossRef]
12. Sari, R.; Piran, T.; Narayan, R. Spectra and Light Curves of Gamma-Ray Burst Afterglows. *Astrophys. J.* **1998**, *497*, L17–L20. [CrossRef]
13. Piran, T. Gamma-Ray Bursts and the Fireball Model. *Phys. Rep.* **1999**, *314*, 575–667. [CrossRef]
14. Lazzati, D.; Covino, S.; Ghisellini, G. On the Role of Extinction in Failed Gamma-Ray Burst optical/IR Afterglows. *Mon. Not. R. Astron. Soc.* **2002**, *330*, 583–590. [CrossRef]
15. Tanvir, N.R.; Levan, A.J.; Rol, E.; Starling, R.L.C.; Gorosabel, J.; Priddey, R.S.; Malesani, D.; Jakobsson, P.; O'Brien, P.T.; Jaunsen, A.O.; et al. The Extreme, Red Afterglow of GRB 060923A: Distance or Dust? *Mon. Not. R. Astron. Soc.* **2008**, *388*, 1743–1750. [CrossRef]
16. Cucchiara, A.; Levan, A.J.; Fox, D.B.; Tanvir, N.R.; Ukwatta, T.N.; Berger, E.; Krühler, T.; Yoldaş, A.K.; Wu, X.F.; Toma, K.; et al. A Photometric Redshift of z 9.4 for GRB 090429B. *Astrophys. J.* **2011**, *736*, 7. [CrossRef]
17. Perley, D.A.; Cenko, S.B.; Bloom, J.S.; Chen, H.W.; Butler, N.R.; Kocevski, D.; Prochaska, J.X.; Brodwin, M.; Glazebrook, K.; Kasliwal, M.M.; et al. The Host Galaxies of Swift Dark Gamma-Ray Bursts: Observational Constraints on Highly Obscured and Very High-Redshift GRBs. *Astron. J.* **2009**, *138*, 1690–1708. [CrossRef]
18. Higgins, A.B.; van der Horst, A.J.; Starling, R.L.C.; Anderson, G.; Perley, D.; van Eerten, H.; Wiersema, K.; Jakobsson, P.; Kouveliotou, C.; Lamb, G.P.; et al. Detailed Multiwavelength Modelling of the Dark GRB 140713A and Its Host Galaxy. *Mon. Not. R. Astron. Soc.* **2019**, *484*, 5245–5255. [CrossRef]
19. Campana, S.; Thone, C.C.; Postigo, A.d.U.; Tagliaferri, G.; Moretti, A.; Covino, S. The X-ray Absorbing Column Densities of Swift Gamma-ray Bursts. *Mon. Not. R. Astron. Soc.* **2010**, *402*, 2429–2435. [CrossRef]
20. Behar, E.; Dado, S.; Dar, A.; Laor, A. CAN The soft X-ray Opacity toward High-Redshift Sources Probe the Missing Baryons? *Astrophys. J.* **2011**, *734*, 26. [CrossRef]
21. Campana, S.; Salvaterra, R.; Melandri, A.; Vergani, S.D.; Covino, S.; D'Avanzo, P.; Fugazza, D.; Ghisellini, G.; Sbarufatti, B.; Tagliaferri, G. The X-ray Absorbing Column Density of a Complete Sample of Bright *Swift* Gamma-Ray Bursts: *Column Densities of Bright Swift GRBs*. *Mon. Not. R. Astron. Soc.* **2012**, *421*, 1697–1702. [CrossRef]
22. Starling, R.L.C.; Willingale, R.; Tanvir, N.R.; Scott, A.E.; Wiersema, K.; O'Brien, P.T.; Levan, A.J.; Stewart, G.C. X-Ray Absorption Evolution in Gamma-Ray Bursts: Intergalactic Medium or Evolutionary Signature of Their Host Galaxies? *Mon. Not. R. Astron. Soc.* **2013**, *431*, 3159–3176. [CrossRef]
23. Efron, B.; Petrosian, V. A Simple Test of Independence for Truncated Data with Applications to Redshift Surveys. *Astrophys. J.* **1992**, *399*, 345. [CrossRef]
24. Efron, B.; Petrosian, V. Nonparametric Methods for Doubly Truncated Data. *J. Am. Stat. Assoc.* **1999**, *94*, 824–834. [CrossRef]
25. Kocevski, D.; Liang, E. Quantifying the Luminosity Evolution in Gamma-Ray Bursts. *Astrophys. J.* **2006**, *642*, 371–381. [CrossRef]

26. Yonetoku, D.; Murakami, T.; Nakamura, T.; Yamazaki, R.; Inoue, A.K.; Ioka, K. Gamma-Ray Burst Formation Rate Inferred from the Spectral Peak Energy–Peak Luminosity Relation. *Astrophys. J.* **2004**, *609*, 935–951. [CrossRef]
27. Singal, J.; Petrosian, V.; Lawrence, A.; Stawarz, Ł. On the Radio and Optical Luminosity Evolution of Quasars. *Astrophys. J.* **2011**, *743*, 104. [CrossRef]
28. Dainotti, M.G.; Petrosian, V.; Singal, J.; Ostrowski, M. Determination of the Intrinsic Luminosity Time Correlation in the X-ray afterglows of Gamma-ray bursts. *Astrophys. J.* **2013**, *774*, 157. [CrossRef]
29. Dainotti, M.G.; Vecchio, R.D.; Shigehiro, N.; Capozziello, S. Selection Effects in Gamma-Ray Burst Correlations: Consequences on the Ratio Between Gamma-ray Burst and Star Formation rates. *Astrophys. J.* **2015**, *800*, 31. [CrossRef]
30. Dainotti, M.G.; Lenart, A.; Sarracino, G.; Nagataki, S.; Capozziello, S.; Fraija, N. The X-ray Fundamental Plane of the Platinum Sample, the Kilonovae and the SNe Ib/c Associated with GRBs. *Astrophys. J.* **2020**, *904*, 97. [CrossRef]
31. Yu, H.; Wang, F.Y.; Dai, Z.G.; Cheng, K.S. An Unexpectedly Low-Redshift Excess of *swift* Gamma-ray Burst Rate. *Astrophys. J. Suppl. Ser.* **2015**, *218*, 13. [CrossRef]
32. Petrosian, V.; Kitanidis, E.; Kocevski, D. Cosmological Evolution of Long Gamma-ray Bursts and Star Formation Rate. *Astrophys. J.* **2015**, *806*, 44. [CrossRef]
33. Pescalli, A.; Ghirlanda, G.; Salvaterra, R.; Ghisellini, G.; Vergani, S.D.; Nappo, F.; Salafia, O.S.; Melandri, A.; Covino, S.; Götz, D. The Rate and Luminosity Function of Long Gamma Ray Bursts. *Astron. Astrophys.* **2016**, *587*, A40. [CrossRef]
34. Lloyd-Ronning, N.M.; Aykutalp, A.; Johnson, J.L. On the Cosmological Evolution of Long Gamma-Ray Burst Properties. *Mon. Not. R. Astron. Soc.* **2019**, *488*, 5823–5832. [CrossRef]
35. Evans, P.A.; Beardmore, A.P.; Page, K.L.; Osborne, J.P.; O'Brien, P.T.; Willingale, R.; Starling, R.L.C.; Burrows, D.N.; Godet, O.; Vetere, L.; et al. Methods and Results of an Automatic Analysis of a Complete Sample of Swift-XRT Observations of GRBs. *Mon. Not. R. Astron. Soc.* **2009**, *397*, 1177–1201. [CrossRef]
36. Chrimes, A.A.; Levan, A.J.; Stanway, E.R.; Lyman, J.D.; Fruchter, A.S.; Jakobsson, P.; O'Brien, P.; Perley, D.A.; Tanvir, N.R.; Wheatley, P.J.; et al. Chandra and Hubble Space Telescope Observations of Dark Gamma-Ray Bursts and Their Host Galaxies. *Mon. Not. R. Astron. Soc.* **2019**, *486*, 3105–3117. [CrossRef]
37. Fynbo, J.P.U.; Jakobsson, P.; Prochaska, J.X.; Malesani, D.; Ledoux, C.; de Ugarte Postigo, A.; Nardini, M.; Vreeswijk, P.M.; Wiersema, K.; Hjorth, J.; et al. Low-Resolution Spectroscopy of Gamma-ray Burst Optical Afterglows: Biases in the *Swift* Sample and Characterization of the Absorbers. *Astrophys. J. Suppl. Ser.* **2009**, *185*, 526–573. [CrossRef]
38. Hashimoto, T.; Ohta, K.; Aoki, K.; Tanaka, I.; Yabe, K.; Kawai, N.; Aoki, W.; Furusawa, H.; Hattori, T.; Iye, M.; et al. "DARK" GRB 080325 in a Dusty Massive Galaxy at z 2. *Astrophys. J.* **2010**, *719*, 378–384. [CrossRef]
39. Burrows, D.N.; Hill, J.E.; Nousek, J.A.; Kennea, J.A.; Wells, A.; Osborne, J.P.; Abbey, A.F.; Beardmore, A.; Mukerjee, K.; Short, A.D.T.; et al. The Swift X-ray Telescope. *Space Sci. Rev.* **2005**, *120*, 165–195. [CrossRef]
40. Dainotti, M.G.; Petrosian, V.; Bowden, L. Cosmological Evolution of the Formation Rate of Short Gamma-Ray Bursts with and Without Extended Emission. *Astrophys. J. Lett.* **2021**, *914*, L40. [CrossRef]
41. Hjorth, J.; Malesani, D.; Jakobsson, P.; Jaunsen, A.O.; Fynbo, J.P.U.; Gorosabel, J.; Krühler, T.; Levan, A.J.; Michałowski, M.J.; Milvang-Jensen, B.; et al. The Optically Unbiased Gamma-ray Burst Host (Tough) Survey. I. Survey Design and Catalogs. *Astrophys. J.* **2012**, *756*, 187. [CrossRef]
42. Perley, D.A.; Levan, A.J.; Tanvir, N.R.; Cenko, S.B.; Bloom, J.S.; Hjorth, J.; Krühler, T.; Filippenko, A.V.; Fruchter, A.; Fynbo, J.P.U.; et al. A Population of Massive, Luminous Galaxies Hosting Heavily Dust-Obscured Gamma-ray bursts: Implications for the Use of Grbs As Tracers of Cosmic Star Formation. *Astrophys. J.* **2013**, *778*, 128. [CrossRef]
43. Levesque, E.M.; Kewley, L.J.; Graham, J.F.; Fruchter, A.S. A high-metallicity host environment for the long-duration GRB 020819. *Astrophys. J.* **2010**, *712*, L26–L30. [CrossRef]
44. Castro-Tirado, A.J.; Bremer, M.; McBreen, S.; Gorosabel, J.; Guziy, S.; Fakthullin, T.A.; Sokolov, V.V.; González Delgado, R.M.; Bihain, G.; Pandey, S.B.; et al. The Dark Nature of GRB 051022 and Its Host Galaxy. *Astron. Astrophys.* **2007**, *475*, 101–107. [CrossRef]
45. Trani, A.A.; Mapelli, M.; Bressan, A. The Impact of Metallicity-Dependent Mass Loss Versus Dynamical Heating on the Early Evolution of Star Clusters. *Mon. Not. R. Astron. Soc.* **2014**, *445*, 1967–1976. [CrossRef]
46. Haislip, J.; Nysewander, M.; Reichart, D.; Levan, A.; Tanvir, N.; Cenko, S.B.; Fox, D.B.; Price, P.A.; Castro-Tirado, A.J.; Gorosabel, J.; et al. AuthA photometric redshift of $z = 6.39 \pm 0.12$ for GRB 050904. *Nature* **2005**, *440*, 181–183. [CrossRef] [PubMed]
47. Niino, Y.; Aoki, K.; Hashimoto, T.; Hattori, T.; Ishikawa, S.; Kashikawa, N.; Kosugi, G.; Onoue, M.; Toshikawa, J.; Yabe, K. The Redshift-Selected Sample of Long Gamma-Ray Burst Host Galaxies: The Overall Metallicity Distribution at z ≪ 0.4. *Publ. Astron. Soc. Jpn.* **2017**, *69*, 27.
48. Cucchiara, A.; Fumagalli, M.; Rafelski, M.; Kocevski, D.; Prochaska, J.X.; Cooke, R.J.; Becker, G.D. Unveiling the Secrets of Metallicity and Massive Star Formation using Dlas along Gamma-ray Bursts. *Astrophys. J.* **2015**, *804*, 51. [CrossRef]
49. Graham, J.F.; Schady, P.; Fruchter, A.S. A Surprising Lack of Metallicity Evolution with Redshift in the Long Gamma-Ray Burst Host Galaxy Population. *Astrophys. J.* **2023**, *954*, 13. [CrossRef]
50. Petrosian, V.; Dainotti, M.G. Progenitors of Low-redshift Gamma-Ray Bursts. *Astrophys. J. Lett.* **2024**, *963*, L12. [CrossRef]
51. Dong, X.F.; Li, X.J.; Zhang, Z.B.; Zhang, X.L. A Comparative Study of Luminosity Functions and Event Rate Densities of Long GRBs with Non-Parametric Method. *Mon. Not. R. Astron. Soc.* **2022**, *513*, 1078–1087. [CrossRef]

52. Bolmer, J.; Greiner, J.; Krühler, T.; Schady, P.; Ledoux, C.; Tanvir, N.R.; Levan, A.J. Dust Reddening and Extinction Curves Toward Gamma-Ray Bursts at $z > 4$. *Astron. Astrophys.* **2018**, *609*, A62. [CrossRef]
53. Cen, R.; Kimm, T. Diverse Properties of Interstellar Medium Embedding Gamma-ray Bursts at the Epoch of Reionization. *Astrophys. J.* **2014**, *794*, 50. [CrossRef]
54. Corre, D.; Buat, V.; Basa, S.; Boissier, S.; Japelj, J.; Palmerio, J.; Salvaterra, R.; Vergani, S.D.; Zafar, T. Investigation of Dust Attenuation and Star Formation Activity in Galaxies Hosting GRBs. *Astron. Astrophys.* **2018**, *617*, A141. [CrossRef]
55. Wilkins, S.M.; Trentham, N.; Hopkins, A.M. The Evolution of Stellar Mass and the Implied Star Formation History. *Mon. Not. R. Astron. Soc.* **2008**, *385*, 687–694. [CrossRef]
56. Nanayakkara, T.; Glazebrook, K.; Kacprzak, G.G.; Yuan, T.; Fisher, D.; Tran, K.V.; Kewley, L.J.; Spitler, L.; Alcorn, L.; Cowley, M.; et al. ZFIRE: Using Hα Equivalent Widths to Investigate the in Situ Initial Mass Function at z 2. *Mon. Not. R. Astron. Soc.* **2017**, *468*, 3071–3108. [CrossRef]
57. Stacy, A.; Greif, T.H.; Bromm, V. The First Stars: Formation of Binaries and Small Multiple Systems. *Mon. Not. R. Astron. Soc.* **2010**, *403*, 45–60. [CrossRef]
58. Toma, K.; Sakamoto, T.; Mészáros, P. Population III Gamma-ray Burst Afterglows: Constraints on Stellar Masses and External Medium Densities. *Astrophys. J.* **2011**, *731*, 127. [CrossRef]
59. Bromm, V.; Loeb, A. High-Redshift Gamma-Ray Bursts from Population III Progenitors. *Astrophys. J.* **2006**, *642*, 382–388. [CrossRef]
60. Campisi, M.A.; Maio, U.; Salvaterra, R.; Ciardi, B. Population III Stars and the Long Gamma-Ray Burst Rate: Population III Stars and LGRBs. *Mon. Not. R. Astron. Soc.* **2011**, *416*, 2760–2767. [CrossRef]
61. Lamb, D.Q.; Reichart, D.E. Gamma-Ray Bursts as a Probe of the Very High Redshift Universe. *Astrophys. J.* **2000**, *536*, 1. [CrossRef]
62. Collaboration, P.; Adam, R.; Aghanim, N.; Ashdown, M.; Aumont, J.; Baccigalupi, C.; Ballardini, M.; Banday, A.J.; Barreiro, R.B.; Bartolo, N.; et al. *Planck* Intermediate Results: XLVII. *Planck* Constraints on Reionization History. *Astron. Astrophys.* **2016**, *596*, A108.
63. Chen, H.W.; Prochaska, J.X.; Gnedin, N.Y. A New Constraint on the Escape Fraction in Distant Galaxies Using γ-Ray Burst Afterglow Spectroscopy. *Astrophys. J.* **2007**, *667*, L125. [CrossRef]
64. Phillips, G.D.; Oey, M.S.; Cuevas, M.; Castro, N.; Kothari, R. Runaway OB Stars in the Small Magellanic Cloud. III. Updated Kinematics and Insights into Dynamical Versus Supernova Ejections. *Astrophys. J.* **2024**, *966*, 243. [CrossRef]
65. Le Floc'h, E.; Charmandaris, V.; Gordon, K.; Forrest, W.J.; Brandl, B.; Schaerer, D.; Dessauges-Zavadsky, M.; Armus, L. THE FIRST INFRARED STUDY OF THE CLOSE ENVIRONMENT OF A LONG GAMMA-RAY BURST. *Astrophys. J.* **2012**, *746*, 7. [CrossRef]
66. Tanvir, N.R.; Le Floc'h, E.; Christensen, L.; Caruana, J.; Salvaterra, R.; Ghirlanda, G.; Ciardi, B.; Maio, U.; D'Odorico, V.; Piedipalumbo, E.; et al. Exploration of the High-Redshift Universe Enabled by THESEUS. *Exp. Astron.* **2021**, *52*, 219–244. [CrossRef]
67. Yonetoku, D.; Mihara, T.; Doi, A.; Sakamoto, T.; Tsumura, K.; Ioka, K.; Amaya, Y.; Arimoto, M.; Enoto, T.; Fujii, T.; et al. High-z Gamma-Ray Bursts Unraveling the Dark Ages and Extreme Space-Time Mission: HiZ-GUNDAM. In Proceedings of the Space Telescopes and Instrumentation 2020: Ultraviolet to Gamma Ray, Online, 14–18 December 2020; p. 318.
68. Lanza, M.L.; Godet, O.; Arcier, B.; Yassine, M.; Atteia, J.L.; Bouchet, L. High-z Gamma-Ray Burst Detection by SVOM/ECLAIRs: Impact of Instrumental Biases on the Bursts' Measured Properties. *Astron. Astrophys.* **2024**, *685*, A163. [CrossRef]